

Dual-probe 1D hybrid fs/ps rotational CARS for simultaneous single-shot temperature, pressure, and O₂/N₂ measurements

DAVID ESCOFET-MARTIN^{1,*}, ANTHONY O. OJO¹, JOSHUA COLLINS¹, NILS TORGE MECKER¹, MARK LINNE¹, AND BRIAN PETERSON¹

¹ Institute for Multiscale Thermofluids, University of Edinburgh, Edinburgh, UK.

*Corresponding author: david.escofet@ed.ac.uk

Compiled February 25, 2022

We employ dual-probe one-dimensional (1D) femtosecond (fs)/picosecond (ps) hybrid rotational coherent anti-Stokes Raman spectroscopy (HRCARS) to investigate simultaneous temperature, pressure, and O₂/N₂ measurements for gas-phase diagnostics. The dual-probe HRCARS technique allows for simultaneous measurements from the time and frequency-domain. A novel approach for measuring pressure, which offers high accuracy (<1%) and precision (0.42%), is presented. The technique is first demonstrated in a chamber for a range of pressures (1-1.5 bar). This technique shows an impressive capability of resolving 1D pressure gradients arising from a N₂ jet impinging on a surface, both in laminar and turbulent conditions. The technique is shown to be capable of resolving single-shot pressure gradients (0.04 bar/mm) originating from kinetic energy conversion to pressure and resolves characteristic O₂/N₂ structures from laminar and turbulent mixing.

© 2022 Optical Society of America

<http://dx.doi.org/10.1364/ao.XX.XXXXXX>

Temperature is a key thermodynamic variable in reactive flows, because chemical reaction rates are exponentially temperature dependent. Spatially resolved pressure relates to molecular motion and forces, and it is critical for aerodynamic studies. Relative species concentrations are essential when evaluating turbulent mixing, which is prevalent in many practical applications where two gases have to be combined. There is thus a need for spatially resolved, one-dimensional (1D) gas-phase measurements of pressure, temperature and species, which would support flow simulations and optimize operation of system components in practical devices such as gas turbines.

Laser techniques for pressure and temperature are non-intrusive [1]. In gas-phase thermometry, coherent anti-Stokes Raman spectroscopy (CARS) is esteemed for measurement pre-

cision and accuracy [2]. Historically, nanosecond (ns) CARS provided zero-dimensional (0D) temperature measurements through highly resolved spectra [3], and simultaneous temperature and pressure measurements were performed by utilizing different spectral features in the frequency-domain [4, 5].

New technological developments such as high energy picosecond (ps) and femtosecond (fs) lasers have granted the extension of CARS measurements from 0D to 1D [6] and to two-dimensional (2D) [7]. These developments permitted time-domain experiments to resolve collisional behavior. Time-resolved CARS has been used to infer Raman coherence decay information [8, 9] and temperature [10, 11].

Encoding time-domain information into the frequency-domain has been done by chirped-probe-pulse (CPP) CARS [12] but remains complex and limited to 0D. Recently, Prince et al [13] introduced hybrid fs/ps CARS (HCARS). This technique employs fs beams for the pump/Stokes and a ps beam for the probe. With fs/ps HCARS, frequency-domain information is time-resolved due to the short ps probe, while time-domain information can be obtained by scanning the probe delay [14, 15]. The significance of this new configuration can be observed in measurements applied in a wide range of pressures, temperatures, and species [14–20]. Multiple-probe HCARS experiments have been demonstrated in 0D to correct temperature for time-varying collisional environments [21]. The frequency-domain pressure dependence of HCARS has been exploited to measure pressure [22]. Using this pressure dependence and multiple probes, simultaneous pressure and temperature measurements were performed in 0D [23] and 1D [24]. However, a trade-off between pressure sensitivity and signal level exists when evaluating pressure [24]. This limits the measurements accuracy and precision. Single-shot temporally and spectrally resolved coherences have been demonstrated in 0D [25], limitations in detector dimensionality complicate 1D measurements.

This Letter introduces a new dual-probe 1D hybrid fs/ps rotational CARS (HRCARS) approach for simultaneous single-shot temperature, pressure, and O₂/N₂ ratio measurements. This analysis exploits the strong time-domain pressure dependence of the CARS signal for accurate and precise pressure measurements and overcomes challenges within the frequency-domain.

The dual-probe 1D fs/ps HRCARS technique is demonstrated

here in two environments. The first is an optically accessible chamber [26] to evaluate the accuracy of the pressure measurements. The second is a high speed N₂ jet impinging on a surface, to demonstrate the utility of the technique in capturing 1D pressure gradients.

Figure 1 illustrates the experimental setup for the N₂ impinging jet. The setup is modified from previous HRCARS experimental layouts [7] to include two probe beams. The seed (Vitara) of a Ti:sapphire amplifier delivering 35 fs pulses with 7.5 mJ at 1 kHz is locked to the ninth harmonic of the oscillator frequency (80 MHz) of a diode pumped Nd:YAG providing 20 ps pulses with 20 mJ at 50 Hz.

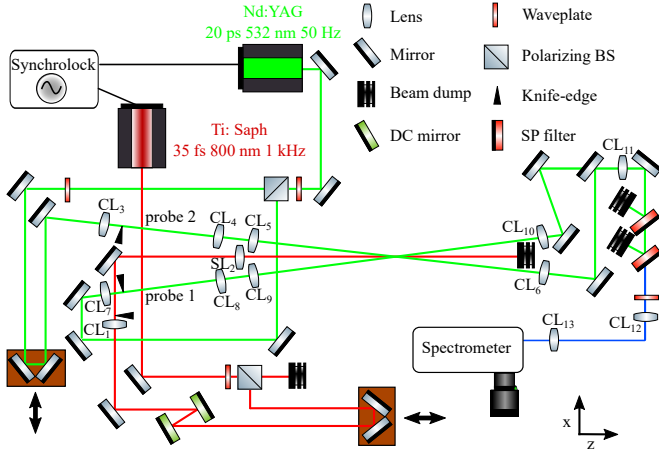


Fig. 1. Schematic of the experimental setup for the N₂ impinging jet measurements.

The pump/Stokes energy is adjusted using a variable attenuator [waveplate plus polarizing beam splitter (BS)]. We use dispersion compensation (DC) mirrors to precompensate for dispersion effects caused by the cylindrical lens (CL)₁ and spherical lens (SL)₂. A compensation of -220 fs^2 provides a near Fourier-transformed pulse after going through the lenses. A combination of a CL₁ ($f_1=300 \text{ mm}$) and a SL₂ ($f_2=300 \text{ mm}$) create a laser sheet that intersects the probe beam sheet. The probe beam is split (with a waveplate plus polarizing BS) into 2 probes: 5% to probe 1 ($\tau_1 \approx 40 \text{ ps}$) and 95% to probe 2 ($\tau_2 \approx 270 \text{ ps}$). Two translation stages are used to control the relative delays between the three beams. Two pairs of CLs_{3,4} ($f_{3,4}=150 \text{ mm}$) and CLs_{7,8} ($f_{7,8}=150 \text{ mm}$), with the optical power aligned with the y axis and separated by $2f$, are placed in the optical path. The CLs_{4,8} image a knife-edge into the probe volume with a magnification slightly < 1 . The knife-edge prevents scattering of the beam from the impinging surface. CLs_{5,9} ($f_{5,9}=250 \text{ mm}$) with the optical power along the x axis create two laser sheets. The laser sheets cross at the probe volume with an angle of 5° with the pump/Stokes. The beams are then collimated with CLs_{6,10} ($f_{6,10}=400 \text{ mm}$). The mirrors placed between the probe volume and CL₁₁ are positioned such that both path lengths are the same. The probe volume ($0.055 \times 1.2 \times 4.5 \text{ mm}^3$, $\Delta x \times \Delta z \times \Delta y$) is relay imaged into the entrance of the spectrometer using CL₁₁ and CL₁₂ ($f_{11}=500 \text{ mm}$, $f_{12}=250 \text{ mm}$). The anti-Stokes and Stokes signals are separated using two angle-tunable short-pass (SP) filters. The CL₁₃ ($f_{13}=100 \text{ mm}$) focuses the light into the spectrometer. The 0.75 m spectrometer is equipped with a 2400 gr/mm grating, which disperses the HRCARS signal onto an electron multiplying charge coupled device (EMCCD). The

dispersion is $0.18 \text{ cm}^{-1}/\text{pixel}$ with a spectral resolution of 0.75 cm^{-1} (FWHM). The magnification of the CLs_{7,8} and CL₁₁ is set to ≈ 0.8 . The EMCCD is binned 2×1 in the y direction and is operated at 25 Hz with 1 ms exposure for a spatial to pixel relationship of $30 \mu\text{m}/\text{pixel}$. Figure 2(a) shows a representative single-shot spectrogram of the CARS intensity, where the two probes are imaged one on top of the other. The resolution of the imaging system is $60 \mu\text{m}$, found by evaluating the sharpness of the imaged knife-edge. A total length of $\approx 4.5 \text{ mm}$ is evaluated from the surface. 1D HRCARS spectrograms are corrected for the finite bandwidth of the pump/Stokes pulses by scanning the probe beam delay with respect to the pump/Stokes in an argon environment. A weighted average from these delays is used to correct the experimental spectrograms.

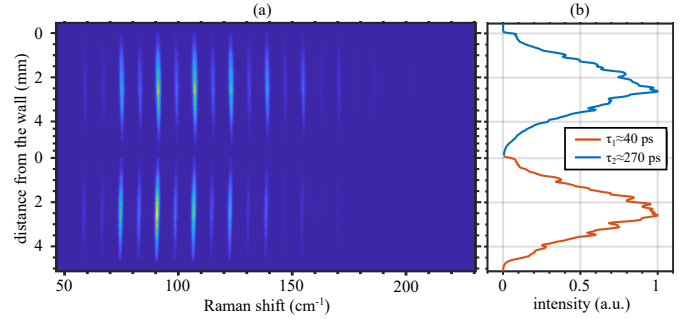


Fig. 2. (a) Single-shot spatially and temporally resolved spectrogram of the dual-probe fs/ps HRCARS near the symmetry axis for the laminar N₂ impinging jet (374x1024 pixels). (b) Single-shot spatially and temporally resolved projected intensity of the dual-probe fs/ps HRCARS.

For the chamber experiments, the aforementioned knife-edges (Fig. 1) together with CLs_{1,3,4,7,8} are removed, and SL₂ is substituted for a CL with $f=300 \text{ mm}$. Due to the increased dispersion from the chamber windows (12 mm fused silica), the number of bounces between the DC mirrors is increased to provide -440 fs^2 . The measured pulse after passing through the window is 37 fs (FWHM). The energy employed for the pump/Stokes beam is significantly reduced (<3 mJ) due to supercontinuum light generation in the chamber windows.

The CARS model used here is detailed in [27, 28]. Pressure dependent linewidths are included with self-broadened linewidths for N₂ [20] and O₂-N₂ for O₂ [29]. For the frequency-domain fitting, a three-dimensional library with varying temperature, pressure, and O₂/N₂ ratio was employed.

The spatially resolved intensities for different probe delays shown in Fig. 2(b) are key to studying the time-domain pressure fitting. The intensity from integrating the CARS signal is

$$I_{\text{CARS}}(T, P, \tau) \propto \int \mathcal{F} \left[P^{(3)}(t, \tau, T, P) \right] d\omega \quad (1)$$

where $P^{(3)}$ is the third order polarization

$$P^{(3)}(t, \tau, T, P) \propto \left(\frac{i}{\hbar} \right)^3 E_{pr}(t - \tau) R_{\text{CARS}}(t, T, P) e^{i\omega_{pr}(t - \tau)}. \quad (2)$$

E_{pr} is the normalized electric field envelope of the probe, τ is the relative delay between the probe and the pump/Stokes, and R_{CARS} is the molecular response function

$$R_{\text{CARS}}(t, T, P) = \frac{P}{kT} \sum_j I_{j,j+2}(T) \times e^{\frac{i}{\hbar} (i\Delta E_{j,j+2} - \frac{1}{2}\Gamma_{j,j+2}(T, P))}, \quad (3)$$

where P/kT represents the number density effect, $I_{J,J+2}$ is the Raman transition strength, $\Delta E_{J,J+2}$ is the frequency of the transitions, and $\Gamma_{J,J+2}$ is the linewidths.

Given electric fields for pump/Stokes and probe, the N₂ HRCARS intensity is a function of probe delay, temperature, and pressure [Eq. (1)-(3)]. Figure 3(a) shows the simulated I_{CARS} for two probe delays ($\tau_1 = 40$ ps, $\tau_2 = 270$ ps) and the I_{ratio}=I_{CARS τ_1} /I_{CARS τ_2} for a range of pressures of 0.9-1.1 bar and temperatures of 280-310 K. The Raman response ($R_{CARS}(t, T, P)$) contains two pressure dependent terms: number density (P/kT) and linewidths ($\Gamma_{J,J+2}(T, P)$). For probe 1 (I_{CARS τ_1} , $\tau_1 = 40$ ps), the number density contribution dominates the signal intensity for both decreasing temperature and increasing pressure. For probe 2 (I_{CARS τ_2} , $\tau_2 = 270$ ps), the signal decreases for increasing pressure due to the exponential dependence on linewidth, which overcomes the quadratic signal increase due to number density.

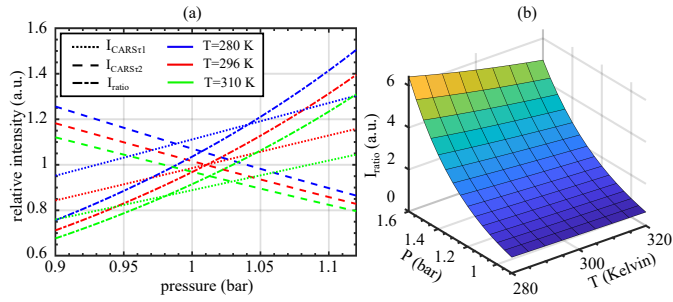


Fig. 3. (a) Simulated intensity as a function of pressure (0.9-1.1 bar) and temperature (280-310 K) for early probe ($\tau_1 = 40$ ps), late probe ($\tau_2 = 270$ ps) and I_{ratio} (b) Simulated relation for I_{ratio} , pressure and temperature.

The I_{ratio} for spatially correlated measurements is not a function of number density or pump/Stokes laser energy, and the pressure sensitivity is increased when compared to any of the individual probes. The relation between the simulated I_{ratio} and the measured I_{ratio} is not complete until a calibration measurement is performed. This accounts for the energy profiles of both individual probe beams, among other things, and is performed separately for chamber and jet experiments, both at ambient pressure (1.01 bar) and temperature. To better utilize the detector dynamic range, the energy split of probes 1 and 2 is adjusted so that $I_{ratio} \approx 1$ under the calibration conditions.

Figure 3(b) shows the simulated normalized I_{ratio} for a range of temperatures of 280-310 K and pressures of 0.9-1.6 bar. The surface plot illustrates the strong sensitivity of the I_{ratio} with respect to pressure; a variation from 1 to 1.6 bar produces an I_{ratio} change greater than five for this temperature range. The I_{ratio} sensitivity with respect to pressure is predominantly a function of $\Delta\tau = \tau_2 - \tau_1$ and can be adjusted to match the expected measured pressure to the dynamic range of the detector.

The fitting procedure starts by assuming ambient pressure in a frequency-domain fit for probe 1, so we obtain temperature (T_1). This temperature is then used to obtain pressure using the I_{ratio} -pressure relation. The calculated pressure is then used to refit probe 1, resulting in the final temperature (T). With the final temperature and the I_{ratio} -pressure relation, we can obtain the final pressure (P) that has already converged. The statistics displayed in Table 1 are for spatially and time-resolved measurements in the chamber, from evaluating the central 20 spectral rows in 50 shots. The measurements precision for the chamber is hindered compared to the N₂ impinging jet experiments due

to the reduced pump/Stokes energy (<3 mJ).

Table 1. Pressure and temperature measurements in the chamber

\overline{T}_1 (K)	\overline{T} (K)	\overline{P} (bar)	$\frac{\sigma_T}{\overline{T}}$ (%)	$\frac{\sigma_P}{\overline{P}}$ (%)	$\overline{P}_{trans.}$ (bar)
296.43	296.43	1.01	1.36	0.83	1.01
298.59	296.59	1.22	1.14	1.29	1.21
299.73	296.87	1.31	1.08	1.72	1.30
300.17	296.64	1.38	1.04	1.91	1.37
301.30	296.83	1.48	0.94	2.44	1.49

T_1 shows a systematic increase of 1.7% as pressure increases 0.47 bar, while the final calculated temperature (\overline{T}) only varies 0.2% in the studied pressure range. The pressure measurements are benchmarked against a pressure transducer ($P_{trans.}$). The agreement between \overline{P} with $P_{trans.}$ is better than 1 %. The temperature precision improves from 1.36 to 0.94% as pressure increases due to the increased signal from I_{CARS τ_1} . The pressure precision decreases from 0.83 to 2.44% as pressure increases, due to the signal decrease from I_{CARS τ_2} .

To demonstrate the utility of the dual-probe HRCARS technique, measurements were applied to a N₂ jet impinging on a surface. The surface is curved along the z direction (d=300 mm) for easier optical access. Measurements are performed under two conditions, $\overline{V}=5.2$ m/s (Re=1,420, laminar) and $\overline{V}=104.2$ m/s (Re=28,510, turbulent). The jet inner diameter is D=4 mm, and the distance between the jet and the surface is H=11 mm, providing a H/D ratio of 2.75. The 4.5 mm closest to the plate are evaluated for temperature, pressure, and O₂/N₂. For every 2D field, twenty 1D measurements are performed, spaced every 200 μ m, covering the radial direction ± 2 mm of the jet impingement. The surface is (4 \times 4.5 mm², $\Delta x \times \Delta y$), and each averaged field contains the analysis of (150 \times 20 \times 100) 0.3 million spectra.

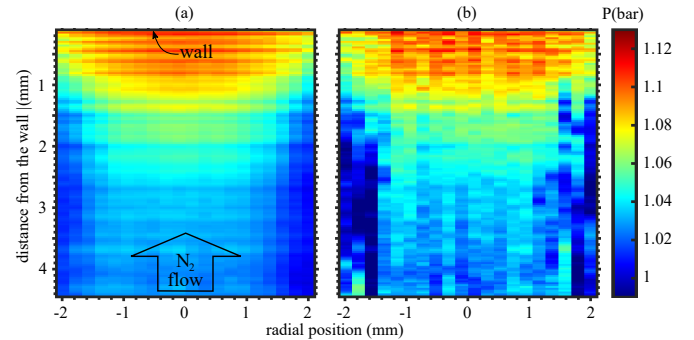


Fig. 4. 2D pressure field from a turbulent (Re=28,510) N₂ jet impinging on a surface: (a) averaged and (b) single-shot.

The laminar pressure field and the laminar and turbulent temperature fields are uniform, thus not shown here. The pressure and temperature fields obtained from the laminar jet are used to evaluate the measurements precision. The spatio-temporal precision for pressure is 0.42% (σ_P/\overline{P}) and for temperature is 0.62% (σ_T/\overline{T}). Figure 4 shows averaged and instantaneous turbulent pressure fields. The maximum measured pressure is ≈ 1.11 bar in both the averaged and single-shot fields. This maximum pressure is located near the symmetry axis close to the surface and

decays both radially and axially. Spatial pressure gradients of the order of 0.04 bar/mm are well-captured.

To further illustrate the jet behavior, Fig. 5 shows both averaged and single-shot O₂/N₂ ratios for both (a), (b) the laminar and (c), (d) the turbulent conditions. The stagnating flow field causes no O₂ detection close to the plate. Comparing both O₂/N₂ averaged fields, the turbulent field has a O₂/N₂ ≈ 0.06 ratio, a three-fold increase due to enhanced air entrainment near the jet radius. Differences in mixing mechanisms are captured in the single-shot measurements: for the laminar jet, the O₂/N₂ measurements show smooth O₂/N₂ gradients typical of mixing dominated mostly by diffusion, while the turbulent jet shows fine structure of air pockets from air entrainment, which also demonstrates the exceptional spatial resolution.

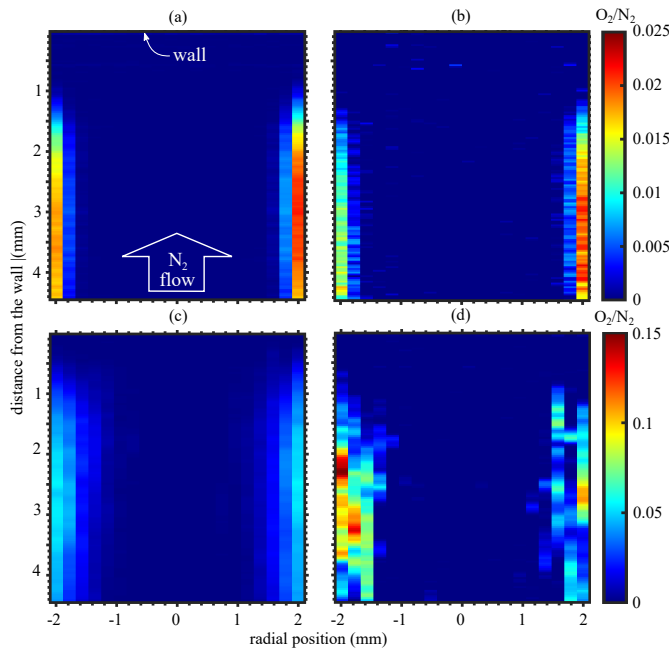


Fig. 5. 2D O₂/N₂ field from a N₂ jet impinging on a surface: laminar jet [(a) averaged field, (b) single-shot field] and turbulent jet [(c) averaged field, (d) single-shot field].

In summary, with dual-probe 1D HRCARS, by extracting information from both the time and frequency-domains, we have demonstrated simultaneous pressure, temperature, and O₂/N₂ ratio measurements. A new methodology to evaluate pressure leads to high accuracy (<1%) for the pressure range 1–1.5 bar, remarkable spatio-temporal temperature precision of 0.62% (σ_T/\bar{T}), unmatched spatio-temporal pressure precision of 0.42% (σ_P/\bar{P}), and fine spatial resolution (0.055 × 1.2 × 0.060 mm³). The pressure measurements are able to describe pressure gradients of the order of 0.04 bar/mm. The O₂/N₂ measurements also capture the spatial characteristics from the mixing interface both in laminar and turbulent conditions. Applying this measurement technique in a more challenging environment with higher pressures, temperatures, and species gradients will be the focus of future work. For such studies, anticipated issues such as reduced signal due to fast collisional dephasing at high pressures, unknown collisional partners, and choice of optimal probe delays will be investigated.

Funding. Engineering and Physical Sciences Research Council (EP/P020593/1, EP/P001661/1); European Research Council

(759546).

Disclosures. The authors declare no conflicts of interest.

REFERENCES

1. A. Y. Chang, B. E. Battles, and R. K. Hanson, Opt. Lett. **15**, 706 (1990).
2. S. Roy, J. R. Gord, and A. K. Patnaik, Prog. Energy Combust. Sci. **36**, 280 (2010).
3. F. Beyrau, T. Seeger, A. Malarski, and A. Leipertz, J. Raman Spectrosc. **34**, 946 (2003).
4. R. E. Foglesong, S. M. Green, R. P. Lucht, and J. C. Dutton, AIAA J. **36**, 234 (1998).
5. R. L. Farrow, R. Trebino, and R. E. Palmer, Appl. Opt. **26**, 331 (1987).
6. C. J. Kliewer, Y. Gao, T. Seeger, B. D. Patterson, R. L. Farrow, and T. B. Settersten, Appl. Opt. **50**, 1770 (2011).
7. A. Bohlin and C. J. Kliewer, J. Chem. Phys. **138** (2013).
8. G. Knopp, P. Beaud, P. Radi, M. Tulej, B. Bougie, D. Cannavo, and T. Gerber, J. Raman Spectrosc. **33**, 861 (2002).
9. V. Morozov, S. Mochalov, A. Olenin, V. Tunkin, and A. Kouzov, J. Raman Spectrosc. **34**, 983 (2003).
10. S. Roy, P. J. Kinnius, R. P. Lucht, and J. R. Gord, Opt. Commun. **36**, 319 (2008).
11. T. Seeger, J. Kiefer, A. Leipertz, B. D. Patterson, C. J. Kliewer, and T. B. Settersten, Opt. Lett. **34**, 3755 (2009).
12. D. R. Richardson, R. P. Lucht, W. D. Kulatilaka, S. Roy, and J. R. Gord, Appl. Phys. B: Lasers Opt. **104**, 699 (2011).
13. B. D. Prince, A. Chakraborty, B. M. Prince, and H. U. Stauffer, J. Chem. Phys. **125** (2006).
14. A. Bohlin, E. Nordström, B. D. Patterson, P. E. Bengtsson, and C. J. Kliewer, J. Chem. Phys. **137** (2012).
15. J. D. Miller, S. Roy, J. R. Gord, and T. R. Meyer, J. Chem. Phys. **135** (2011).
16. J. D. Miller, S. Roy, M. N. Slipchenko, J. R. Gord, and T. Meyer, Opt. express **19**, 15627 (2011).
17. N. T. Mecker, T. L. Courtney, B. D. Patterson, D. Escofet-Martin, B. Peterson, C. J. Kliewer, and M. Linne, J. Opt. Soc. Am. B **37**, 1035 (2020).
18. J. D. Miller, C. E. Dedic, and T. R. Meyer, J. Raman Spectrosc. **46**, 702 (2015).
19. W. D. Kulatilaka, P. S. Hsu, H. U. Stauffer, J. R. Gord, and S. Roy, Appl. Phys. Lett. **97**, 1 (2010).
20. C. J. Kliewer, A. Bohlin, E. Nordström, B. D. Patterson, P. E. Bengtsson, and T. B. Settersten, Appl. Phys. B: Lasers Opt. **108**, 419 (2012).
21. B. D. Patterson, Y. Gao, T. Seeger, and C. J. Kliewer, Opt. Lett. **38**, 4566 (2013).
22. S. P. Kearney and P. M. Danehy, Opt. Lett. **40**, 4082 (2015).
23. C. E. Dedic, A. D. Cutler, and P. M. Danehy, AIAA Scitech 2019 Forum (2019).
24. S. P. Kearney, D. R. Richardson, J. E. Retter, C. E. Dedic, and P. M. Danehy, AIAA Scitech 2020 Forum (2020).
25. A. Hosseini, M. Ruchkina, P. Ding, P.-E. Bengtsson, and J. Bood, Opt. Lett. **45**, 308 (2020).
26. D. Escofet-Martin, A. O. Ojo, N. T. Mecker, M. A. Linne, and B. Peterson, Proc. Combust. Inst. 38, accepted for publication (2021), doi:10.1016/j.proci.2020.06.097.
27. C. Yang, D. Escofet-Martin, D. Dunn-Rankin, Y. C. Chien, X. Yu, and S. Mukamel, J. Raman Spectrosc. **48**, 1881 (2017).
28. C. Yang, P. He, D. Escofet-Martin, J.-B. Peng, R.-W. Fan, X. Yu, and D. Dunn-Rankin, Appl. Opt. **57**, 197 (2018).
29. G. Millot, R. Saint-Loup, J. Santos, R. Chaux, H. Berger, and J. Bonamy, The J. Chem. Phys. **96**, 961 (1992).